*J. Fluid Mech.* (1998), *vol.* 360, *pp.* 273–294. Printed in the United Kingdom



# Monopolar vortices in an irrotational annular shear flow

By R. R. TRIELING†, A. H. LINSSEN AND G. J. F. VAN HEIJST

Fluid Dynamics Laboratory, Department of Technical Physics, Eindhoven University of Technology, PO Box 513, 5600 MB Eindhoven, The Netherlands

(Received 11 April 1997 and in revised form 8 December 1997)

The evolution characteristics of monopolar vortices in an irrotational annular shear flow were investigated both experimentally and theoretically. The background flow was generated in a rotating tank by an appropriate source–sink configuration, while the monopolar vortex was created by withdrawing fluid for a short time. Dye-visualization studies demonstrated the gradual destruction of the vortex through a process called 'vortex stripping', i.e. long filaments of passive tracers were being shed from the edge of the vortex. In contrast to uniform shear flows, these filaments were asymmetrically attached to the vortex core. Furthermore, the vortex was observed to evolve in a quasi-stationary manner until its final indefinite breaking. The asymmetric stripping process could be explained by modelling both the monopolar vortex and the ambient flow simply by point vortices, and by adopting the method of contour kinematics to trace material contours in the velocity field induced by the point vortices. Furthermore, the effect of a continuous spatial vorticity distribution was investigated by applying the contour dynamics technique, in which the vortex is represented by a stack of uniform vorticity patches. The observed vortex evolution could be well captured by this latter approach.

## 1. Introduction

The large-scale motions in the atmosphere and the ocean may be considered as two-dimensional owing to the geometrical constraints and the rotation of the Earth. Also density stratification may contribute to the two-dimensionality of these geophysical flows. Satellite observations have revealed the presence of large-scale vortical structures, such as the low- and high-pressure areas and oceanic eddies. Numerical studies have confirmed the formation of coherent structures in two-dimensional flow domains (see for example McWilliams 1984 and Legras, Santangelo & Benzi 1988).

Two-dimensional vortices may be distorted by mutual interaction. Owing to their generally compact shape, vorticity is mainly concentrated in the core of each vortex. If these vortices come close to each other, they will inevitably merge (see e.g. Overman & Zabusky 1982 and Melander, Zabusky & McWilliams 1988). However, as long as they are relatively far apart, they may feel a shearing background flow that is essentially irrotational.

† Present address: Royal Netherlands Meteorological Institute, PO Box 201, 3730 AE De Bilt, The Netherlands.

Recently, the behaviour of two-dimensional vortices in shear flows has been investigated intensively, especially in numerical studies. Contour dynamics simulations by Dritschel (1989) and Legras & Dritschel (1993, 1994) have revealed the so-called 'stripping' of distributed vortices in uniform shear flows, i.e. the removal of weak vorticity from the edge of the vortex, leading to the appearance of long vorticity filaments which are carried away by the ambient flow. However, not much attention has been paid so far to the behaviour of a monopolar vortex in an irrotational shear flow.

Therefore, in the present paper, the evolution of a monopolar vortex in an irrotational annular shear flow will be investigated, both experimentally and theoretically. The laboratory experiments were performed in a rotating tank. The ambient flow was generated by an appropriate source–sink configuration, whereas the monopolar vortex was created by locally withdrawing fluid for a short time. Apart from flow-visualization studies, which were necessary to observe the qualitative behaviour of the flow field, quantitative information was obtained by video recordings of small tracer particles. Image analysis techniques were used to measure vorticity distributions and to follow individual particles.

It will be shown that the vortex evolution is characterized by the asymmetric shedding of long filaments. Theoretically, this behaviour can be explained by modelling both the monopolar vortex and the irrotational annular shear flow by point vortices, and by applying the so-called contour kinematics method to follow contours of passive tracers. Since the point vortex contains vorticity in one singular point only, whereas real vortices have essentially distributed vorticity, the effect of the distributed vorticity was investigated by adopting the contour dynamics approach.

This paper is organized as follows. In § 2, a theoretical description will be given of the irrotational shear flow induced by the source–sink arrangement, followed by a description of the laboratory set-up in § 3. After that, the laboratory observations will be presented in § 4, in which the characteristics of both the shear flow and the monopolar vortex will be investigated separately. In this section, the evolution of the monopolar vortex in the annular shear flow will also be discussed. In § 5, the observed vortex-stripping process will be explained kinematically by the contour kinematics model. In addition, the effect of distributed vorticity will be discussed in § 6, where the results obtained by the contour kinematics technique will be compared with those obtained by contour dynamics calculations. Finally, in § 7, the main results will be discussed and the conclusions will be given.

## 2. Theoretical description of the source–sink flow

Consider the following source–sink configuration in a system that rotates at an angular velocity $\Omega$ about the vertical axis of symmetry (figure 1). Fluid is injected axisymmetrically at a flow rate $Q$ through a ring-shaped line source in the bottom corner, whereas the same amount of fluid is withdrawn through a sink which is positioned in the centre of the tank.

In view of the axisymmetric shape of the flow domain, it is useful to refer to a cylindrical coordinate system $(r, \theta, z)$, with the corresponding velocity components $(u, v, w)$. The rotation vector $\boldsymbol{\Omega}$ is taken along the $z$-axis. For convenience, the lengths and velocities will be non-dimensionalized by a typical length scale $L$ and some characteristic velocity $U$, respectively, whereas the dimensionless volumetric flow rate

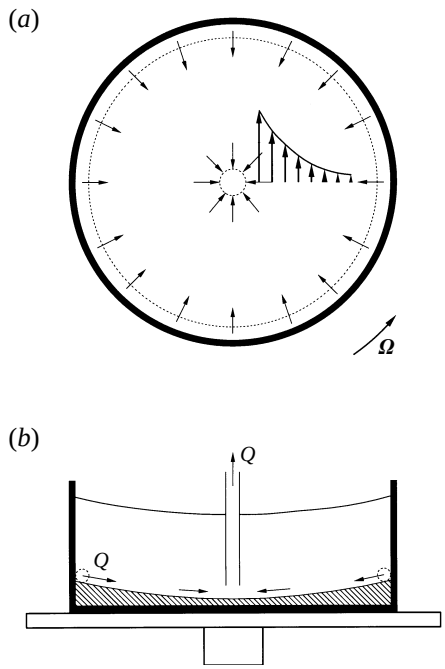


FIGURE 1. Schematic drawing of the experimental set-up for the generation of the annular shear flow: (*a*) top view and (*b*) side view. The container is placed on a turntable, which rotates with an angular velocity $\Omega$. Fluid is injected axisymmetrically with a constant flow rate $Q$ through a ring-shaped line source in the bottom corner, whereas the same amount of fluid is withdrawn by a sink in the centre of the tank. The thin arrows indicate the direction of the $O(E^{1/2})$ transport, whereas the heavy arrows denote the $O(1)$ interior velocity field. The parabolic bottom is indicated by the hatched area.

$Q^*$ is defined by

$$Q^* = Q/(UL^2E^{1/2}), \tag{2.1}$$

where $Q$ is the dimensional flow rate and $E$ is the Ekman number defined below.

Relative to a co-rotating reference frame, with constant angular velocity $\Omega$, the stationary flow is governed by the equations of momentum and conservation of mass, which are given in dimensionless form by

$$Ro\,(\boldsymbol{v}^* \cdot \nabla^*)\boldsymbol{v}^* + 2\boldsymbol{k}^* \times \boldsymbol{v}^* = -\nabla^* p^* + E(\nabla^*)^2\boldsymbol{v}^*, \tag{2.2}$$

$$\nabla^* \cdot \boldsymbol{v}^* = 0, \tag{2.3}$$

respectively, with $\boldsymbol{v}^*$ the velocity vector in the rotating frame, $p^*$ the reduced pressure and $\boldsymbol{k}^* = \boldsymbol{\Omega}/\Omega$ a unit vector in the axial direction. Note that the fluid is assumed to be incompressible and homogeneous. The dimensionless parameters $Ro$ and $E$ in (2.2) are the Rossby number and the Ekman number, defined as

$$Ro = U/(\Omega L), \tag{2.4}$$

$$E = \nu/(\Omega L^2), \tag{2.5}$$

respectively.

It is assumed that the fluid motion is slow compared to the angular velocity of the system, so that the nonlinear terms in (2.2) can be neglected, i.e. $Ro \ll 1$. Moreover,

viscous effects are assumed to be small ($E \ll 1$), which implies that the system is rapidly rotating.

In this system, three different regions may be distinguished. At some distance from the solid walls, the fluid is not affected by viscosity, and is governed by a geostrophic balance of forces:

$$2\boldsymbol{k}^* \times \boldsymbol{v}_I^* = -\nabla p_I^*, \tag{2.6}$$

where the index $I$ refers to the 'interior' domain. The geostrophic balance (2.6) and the continuity equation (2.3) imply that $\partial \boldsymbol{v}_I^*/\partial z = 0$. In order to satisfy the no-slip boundary conditions, an Ekman layer of thickness $\delta_E^* = E^{1/2}$ arises at the bottom wall, whereas a Stewartson layer of thickness $\delta_S^* = E^{1/4}$ is present at the sidewall (see Stewartson 1957). It will be assumed that the air drag is identically zero, so that no boundary layer is present at the free surface.

From the azimuthal component of (2.6), with $\partial/\partial\theta = 0$, it follows that $u_I^* = 0$. Moreover, the normal velocity at the free surface requires that $w_I^* = 0$. Therefore, the interior flow is characterized by a purely azimuthal motion. This implies that the radial $O(E^{1/2})$ transport from the source to the sink has to be carried completely by the Ekman layer at the bottom wall. From linear Ekman dynamics (see e.g. Greenspan 1968) it can be derived that in the Ekman layer the local radial $O(E^{1/2})$ flux per unit length of circumference is given by

$$\tilde{Q}_E^* = \tfrac{1}{2} v_I^*. \tag{2.7}$$

Consequently, the azimuthal interior velocity field is given by

$$v_I^* = Q^*/(\pi r^*), \tag{2.8}$$

or in dimensional form:

$$v_I = \gamma_s / r, \tag{2.9}$$

where

$$\gamma_s \equiv Q\pi^{-1} \left(\Omega/\nu\right)^{1/2}. \tag{2.10}$$

Obviously, the induced motion in the interior domain is equivalent to a potential vortex of strength $\gamma_s$ (the factor $2\pi$ has been included in the definition of $\gamma_s$). It is also apparent that the strength $\gamma_s$ is proportional to the flow rate $Q$. In the subsequent analysis, the index $I$ will be omitted.

## 3. Experimental arrangement

The experiments were performed in a cylindrical tank that was placed on top of a rotating table (see figure 1). The tank was filled with water, the fluid depth being typically 18 cm, and the angular velocity $\Omega$ of the turntable was set to 0.70 rad s$^{-1}$. Either a flat-bottomed container was used (inner diameter 92 cm and depth 35 cm) or a tank with a parabolic bottom (inner diameter 98 cm and depth 25 cm). The parabolic bottom was applied to mimic the shape of the free surface. In this way, a uniform fluid depth was established in order to avoid topographic vorticity production (by stretching or squeezing of fluid columns). Since a parabolic bottom is not required for purely azimuthal flows (see Hide 1977), the shear flow measurements were carried out in the flat-bottomed container.

### 3.1. *Shear flow generation*

Fluid was injected axisymmetrically at the sidewall through a ring-shaped tube (of inner diameter 8 mm), which was positioned in the bottom corner of the tank. The

tube was perforated with small holes of diameter 1–1.5 mm, every 2 cm along the circumference. Fluid was withdrawn through a narrow Perspex tube of inner diameter 10 mm, which was placed vertically along the rotation axis at the centre of the tank. The open end of the sink tube was positioned typically 10 mm above the tank bottom. A pump was used to circulate the fluid through the container with a constant flow rate $Q$. The flow rate was varied between 1.0 and 10.5 ml s$^{-1}$, and the fluctuations in $Q$ were measured to be less than 0.2 ml s$^{-1}$. A similar generation technique was used in a detailed experimental study by Hide (1968), in which a variety of source–sink configurations were discussed. Source–sink flows have also been investigated, either analytically or experimentally, by e.g. Kuo & Veronis (1971), van Heijst (1984) and Brickman & Ruddick (1990).

### 3.2. *Monopole generation*

A cyclonic vortex was created by locally withdrawing fluid through a perforated Perspex tube, with inner diameter 10 mm and outer diameter 15 mm, which was positioned vertically in the fluid. The tube contained 248 small holes of diameter 2 mm, which were distributed uniformly over a length of 15 cm. The fluid was removed by syphoning with a typical flow rate $q = 40$ ml s$^{-1}$ and a typical forcing period $\delta t = 10$ s. Owing to the presence of the Coriolis force, the radial motion induced by the sink was deflected in a cyclonic direction. After the forcing was stopped and the tube was removed from the tank, a well-defined swirling motion was established within a few rotation periods.

### 3.3. *Flow visualization and measurements*

The free surface of the fluid was seeded with small tracer particles in order to obtain quantitative information about the interior velocity field. The motion of the floating particles was monitored continuously by a video camera, which was mounted in the rotating frame at some distance above the tank. After the experiment was finished, the velocity field could be determined at successive times by the particle-tracking package DigImage, developed by Dalziel (1992). Next, the measured velocity field was interpolated on a mesh of $30 \times 30$ grid points (see Paihua Montes 1978 and Nguyen Duc & Sommeria 1988), which was convenient for calculating numerically the distributions of both the vorticity and the stream function. Furthermore, fluorescent dye was added to the fluid to study the qualitative behaviour of the flow field.

## 4. Laboratory observations

### 4.1. *Shear flow characteristics*

In figure 2, the interior velocity components are plotted versus the radial distance $r$ for a typical annular shear flow which was generated by the source–sink arrangement as described in § 3. Each data point corresponds to a velocity vector as obtained by the digitized particle streaks. Only velocity vectors corresponding to the interior region were considered, i.e. the flow within the Stewartson layers was neglected. The scatter in the observed data is probably due to the measurement inaccuracy and small disturbances at the free surface, as well as deviations from axisymmetry of the shear flow. In order to confirm that the interior flow was essentially two-dimensional, some dye-producing crystals were dropped on the free surface of the rotating fluid. The vertical dye streaks originating from these crystals demonstrated that the velocity in the interior region was indeed depth independent. The observed distribution of azimuthal velocity, see figure 2 (*a*), was least-square fitted with (2.9) (solid line),

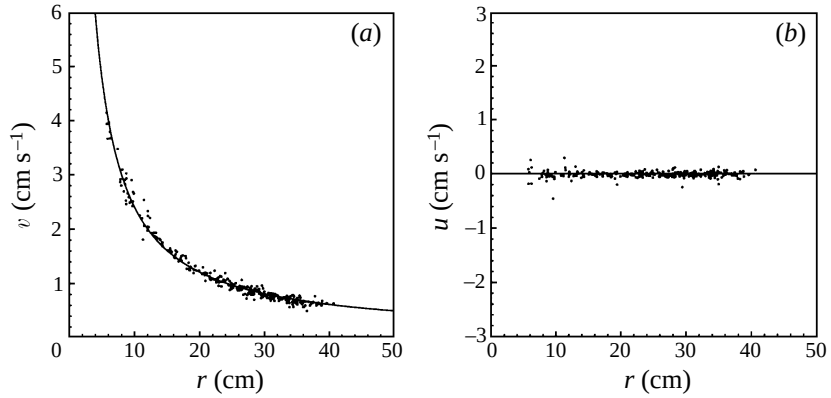


FIGURE 2. Radial distributions of the interior velocity components associated with the annular shear flow, 23 min after the forcing was started: (*a*) azimuthal component $v$ and (*b*) radial component $u$. The experimental data are indicated by dots, whereas the least-square fit with (2.9) is represented by the curved solid line. Based on (2.9), the strength of the shear flow was found to be equal to $24.1 \pm 0.1$ cm$^2$ s$^{-1}$. Experimental parameters: $Q = 10.0$ ml s$^{-1}$ and $H = 17.5$ cm.

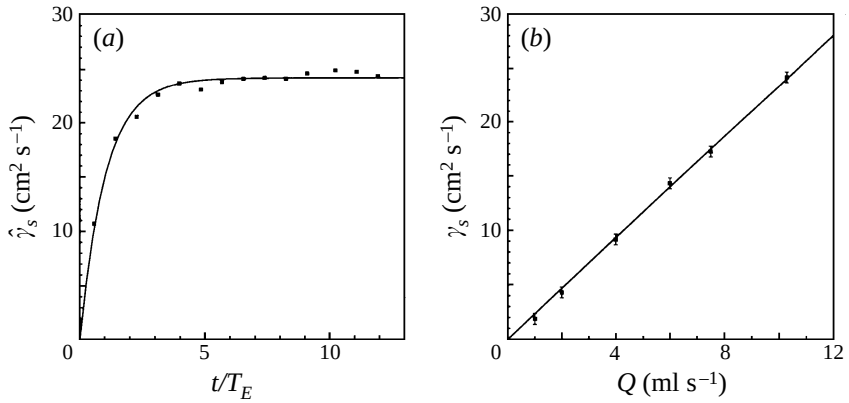


FIGURE 3. (*a*) Time evolution of the instantaneous shear flow strength $\hat{\gamma}_s$ with $T_E = 211$ s. The measured data (squares) are least-square fitted with (4.1). (*b*) Relationship between the strength $\gamma_s$ of the stationary shear flow and the volumetric flux rate $Q$. The measured data (squares) are least-square fitted with the relation $\gamma_s = \alpha Q$. Experimental parameters: $Q = 10.0$ ml s$^{-1}$ (frame *a*) and $H = 17.5$ cm.

where $\hat{\gamma}_s$ was taken as a free parameter, and a very good agreement was obtained. (Here, the hat-symbol is added in order to distinguish between the instantaneous shear flow strength $\hat{\gamma}_s$ and the stationary value $\gamma_s$.) Furthermore, it can be inferred from figure 2(*b*) that the radial velocity is of the same order as the scatter in the experimental data, which is in agreement with the theoretical relation $u = 0$.

The spin-up behaviour of the shear flow was investigated by calculating the strength $\hat{\gamma}_s$ at successive times with a least-square fit as shown in figure 2(*a*). Based on these individual fits, the experimental error in $\hat{\gamma}_s$ was estimated to be 0.1 cm$^2$ s$^{-1}$. The measured time evolution of $\hat{\gamma}_s$ is plotted in figure 3(*a*) as well as a least-square fit according to

$$\hat{\gamma}_s = \gamma_s \left[1 - \exp\left(-t/\tau_s\right)\right], \tag{4.1}$$

where the free parameters $\gamma_s$ and $\tau_s$ represent the stationary strength and the char-

acteristic time scale, respectively. It can be seen that the curve closely matches the experimental data. The corresponding time scale $\tau_s$ was found to be equal to $218 \pm 10$ s. The deviations from (4.1) are probably due to small fluctuations in $Q$, since the error in $\hat{\gamma}_s$ is far too small to account for these deviations. According to linear Ekman dynamics (see e.g. Greenspan 1968), the time evolution in rotating flow systems is characterized by the e-folding Ekman time

$$T_E = H/(\nu\Omega)^{1/2}, \tag{4.2}$$

where $H$ represents the (mean) fluid depth. Taking the experimental values $H = 17.5$ cm, $\Omega = 0.70$ rad s$^{-1}$ and $\nu = 0.98 \times 10^{-2}$ cm$^2$ s$^{-1}$ (for a temperature of 21°C) yields $T_E = 211$ s, which is very close to the observed time scale $\tau_s$. It can be derived from figure 3(*a*) that the flow has reached a stationary state after typically $t = 6T_E \approx 20$ min.

According to (2.10), the stationary strength $\gamma_s$ is proportional to the volumetric flux rate $Q$. This assertion was checked by generating several shear flows with different flux rates $Q$, while the angular velocity $\Omega$ was held constant at 0.70 rad s$^{-1}$ and the temperature was close to 20°C. The strength $\gamma_s$ was obtained by taking the average of three instantaneous strengths $\hat{\gamma}_s$ which were determined at $t = 30$, 35 and 40 min, respectively. In figure 3(*b*), $\gamma_s$ is plotted as a function of $Q$, and the linear relationship is obvious. A linear least-square fit (solid line) was applied to the observed data with the relation $\gamma_s = \alpha Q$. The experimental value $\alpha = 2.33 \pm 0.02$ cm$^{-1}$ is close to the corresponding theoretical value $\alpha = \pi^{-1}(\Omega/\nu)^{1/2} = 2.66$ cm$^{-1}$. The systematic deviation may be explained by the shear stress at the free surface. Owing to the rapid rotation of the container, air drag may slow down the motion of the tracer particles at the free surface.

Also an anticyclonic shear flow was generated by simply reversing the direction of flow through the tank, i.e. fluid was injected through a source in the centre of the tank and withdrawn through a sink at the sidewall. Apart from the direction of the azimuthal flow, similar results were obtained to those related to the cyclonic shear flow.

### 4.2. *Monopolar vortex characteristics in a still ambient fluid*

In figure 4, typical measured distributions of velocity $v$ and vorticity $\omega$ are plotted along a line through the centre of the monopolar vortex, where $s$ denotes the spatial coordinate and $s = 0$ is defined as the vortex centre. The vortex was generated in a still ambient fluid by the method described in § 3. The experimental data are indicated by the symbols. The velocity $v$ corresponds to the velocity component directed perpendicular to the cross-section. It is apparent that the vortex is characterized by a core of single-signed vorticity, which is maximum in the centre, with hardly any negative vorticity around it, i.e. the induced flow has net circulation. This observation can be easily understood from the generation method. Consider the change in the circulation $\Gamma$ around a material contour $C$ which encloses the sink tube by which the vortex is generated. For a barotropic and inviscid fluid, the change in the circulation can be written as

$$\frac{\mathrm{D}\Gamma}{\mathrm{D}t} = -2 \oint_C (\boldsymbol{\Omega} \times \boldsymbol{v}) \cdot \mathrm{d}\boldsymbol{s} = -2\Omega q, \tag{4.3}$$

with $\mathrm{d}\boldsymbol{s}$ an infinitesimal segment of the contour $C$. This equation expresses the production of vorticity by the presence of the Coriolis force. Since the sink induces a radially inward motion, $q$ will be negative so that $\mathrm{D}\Gamma/\mathrm{D}t > 0$ until a quasi-geostrophic motion is established after the forcing is stopped.

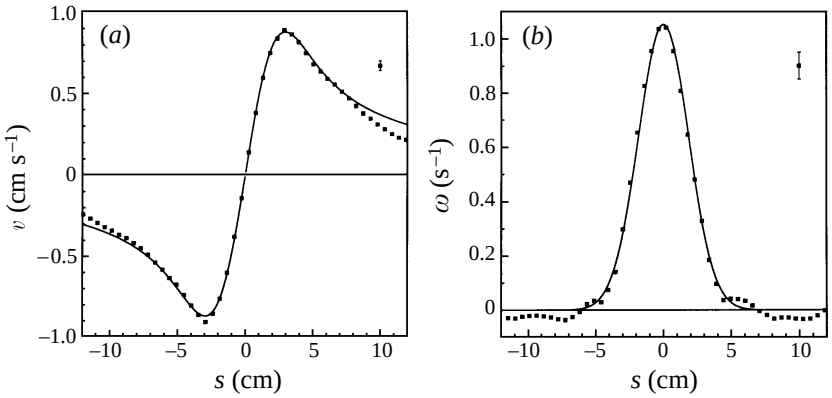


FIGURE 4. Radial cross-sectional distributions of ($a$) the velocity $v$ directed perpendicular to the cross-section and ($b$) the vorticity $\omega$ of a sink-induced cyclonic vortex, at $t/T_E = 0.27$ with $T_E = 220$ s (the forcing was stopped at $t = 0$). The experimental data (squares) corresponding to $|s| \leqslant 5$ cm were least-square fitted with (4.5) and (4.4), respectively, which yielded $\gamma_v = 3.61 \pm 0.08$ cm$^2$ s$^{-1}$ and $r_m = 2.9 \pm 0.1$ cm. Experimental parameters: $q = 40$ ml s$^{-1}$, $\delta t = 10$ s and $H = 19.0$ cm.

The measured velocity profile is observed to be approximately linear in the core of the vortex, whereas at larger radii the velocity decreases relatively slowly towards zero. In figure 4, the measured distributions in the vortex core ($|s| \leqslant 5$ cm) can be accurately fitted by the instantaneous profiles (solid lines) of the so-called Lamb vortex

$$\omega = \frac{2\gamma_v}{L_v^2} \exp\left(-s^2/L_v^2\right) \tag{4.4}$$

and

$$v = \frac{\gamma_v}{s}\left[1 - \exp\left(-s^2/L_v^2\right)\right], \tag{4.5}$$

respectively, where $\gamma_v$ represents the total circulation of the vortex (apart from a factor $2\pi$). In fact, this solution can be considered as a 'snap-shot' of a viscously decaying point vortex at some time $t$, which was analysed by Oseen in 1911 (for details, see Lamb 1932). The characteristic length scale $L_v$ is a measure of the vortex radius and can be related to the radius of peak velocity $r_m$ by the relation $r_m = 1.12L_v$.

The time evolution of stable barotropic vortices has been accurately described by Kloosterziel & van Heijst (1992). Based on their rotating fluid experiments, it was found that for small Rossby numbers the decay of the vortex velocity field is close to exponential, as expected from linear Ekman dynamics. However, their experiments also showed that under typical laboratory circumstances the initial Rossby number is $O(1)$, so that nonlinear effects are important then: the initial stage of the vortex evolution was characterized by a steepening of the velocity profiles and a faster decay rate as compared to linear Ekman decay.

Despite this initial steepening, the results in figure 4 show that in the vortex core the velocity and vorticity distributions can be accurately represented by (4.4) and (4.5). Similar observations were made for later times.

### 4.3. *Evolution of the monopolar vortex in the shear flow*

The typical evolution of the sink vortex in the annular shear flow is illustrated by the series of video images in figure 5. The vortex was created halfway between the

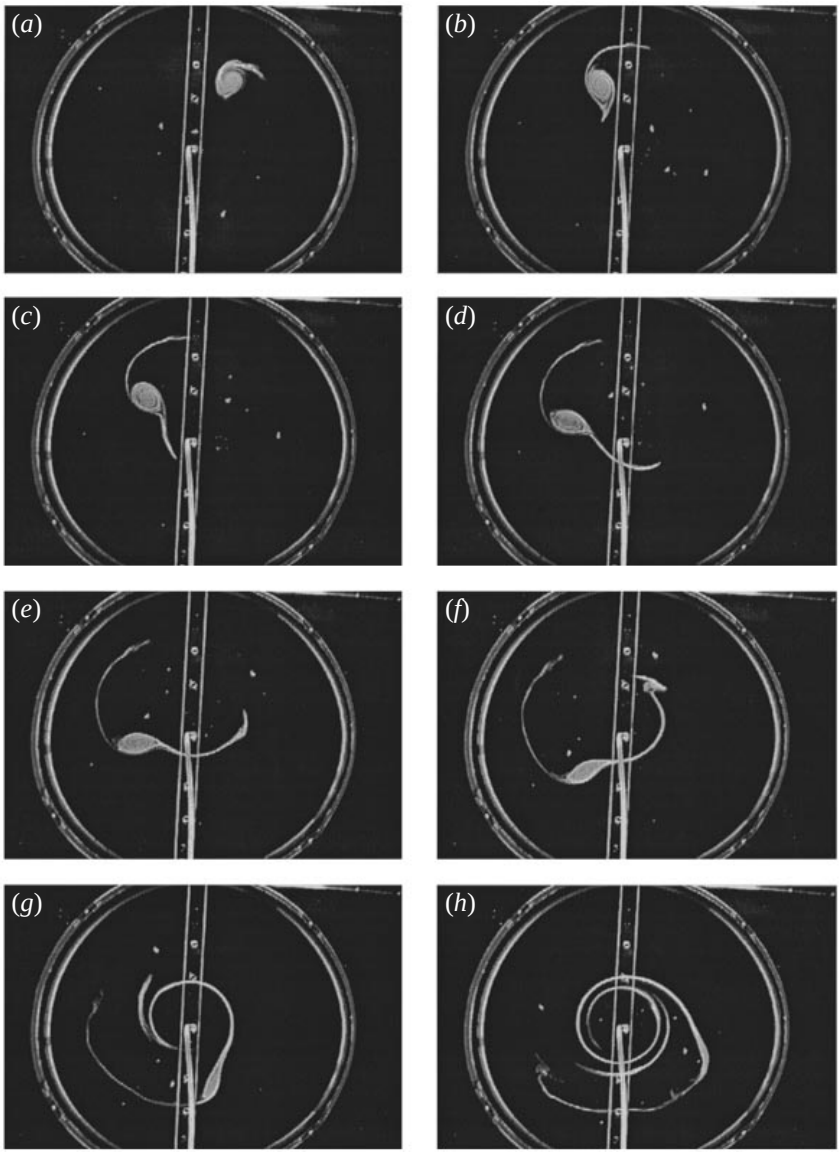


FIGURE 5. Dye visualization of a monopolar vortex in an annular shear flow at successive times after the removal of the sink tube: (*a*) $t/T_E = 0.13$, (*b*) 0.24, (*c*) 0.29, (*d*) 0.34, (*e*) 0.39, (*f*) 0.45, (*g*) 0.55 and (*h*) 0.71, where the Ekman time $T_E = 190$ s. The vortex was coloured with dye between $t/T_E = 0$ and 0.10. Experimental parameters: $Q = 10.5$ ml s$^{-1}$, $q = 40$ ml s$^{-1}$, $\delta t = 10$ s and $H = 16$ cm.

centre and the sidewall of the tank. Shortly after the vortex forcing was stopped and the tube was removed from the tank, the vortex was visualized with fluorescent dye. It is clear from figure 5 that the vortex is advected in a cyclonic direction, while in the meantime, the vortex is being deformed into an oval-like shape. Moreover, the evolution is characterized by the appearance of dye filaments on both sides of the vortex. In the initial stage, see (*a*), one filament is expelled into the ambient fluid, followed by a second filament which arises on the front side of the vortex (see *b, c*). Close inspection of the flow pattern reveals that the filament at the rear of the vortex

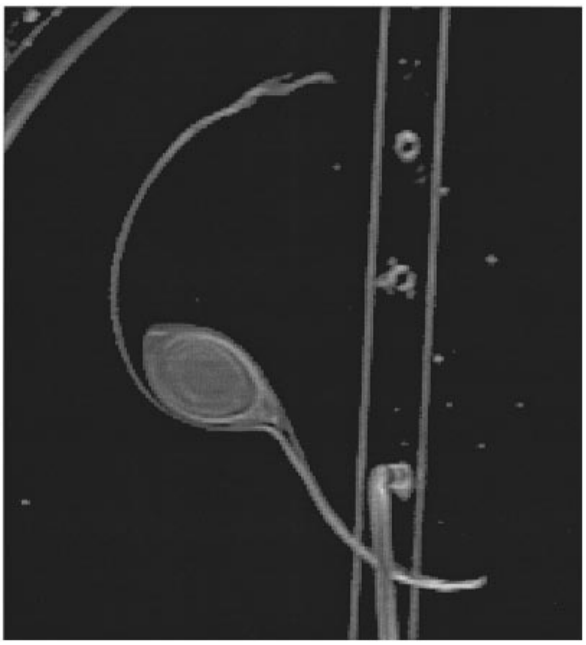

FIGURE 6. Enlarged digitized video image showing the asymmetric stripping of the monopolar vortex at $t/T_E = 0.32$, with $T_E = 190$ s. Experimental parameters as in figure 5.

extends towards the second filament at the front. This can also be observed in figure 6, where a detailed video image is shown of the deformed vortex, along with the two filaments. Similar long vorticity filaments have been observed in numerical studies on the interaction of two monopolar vortices of like-signed vorticity (see e.g. Melander, Zabusky & McWilliams 1987 and Dritschel & Waugh 1992). As time proceeds, a right-angled cusp appears in the dye pattern associated with the vortex core, see (*d*), which soon develops into a tail which is later swept away along the filament at the rear of the vortex (see *e,f*). Note that until this stage, the vortex core is oriented perpendicular to the flow direction of the annular shear. In the final stage, however, the vortex is completely torn apart while being wrapped around the sink in the centre of the tank, as can be observed in (*g,h*).

## 5. Kinematic description of vortex stripping

In order to explain the observed stripping process discussed in § 4, the monopolar vortex will be modelled by a point vortex ($P_v$) with strength $\gamma_v$. Moreover, it was shown in § 2 that the interior velocity field induced by the source–sink configuration is equivalent to that of a potential vortex, the strength of which, $\gamma_s$, is determined by (2.10). Therefore, the ambient flow can also be represented by a point vortex ($P_s$) which is forced to remain fixed in the origin (see figure 7). Point vortex $P_v$ is located at $(x_0, y_0)$ and is passively advected under the action of $P_s$ for an infinite domain. In principle, the boundaries of the laboratory flow domain may be included by using the method of images. However, the velocities induced by the image vortices are negligible provided that $\gamma_v/\gamma_s$ is sufficiently small and $P_v$ does not approach the boundaries too closely. Since both conditions are satisfied in the laboratory experiments, the effects of the boundaries will be neglected in the present analysis.

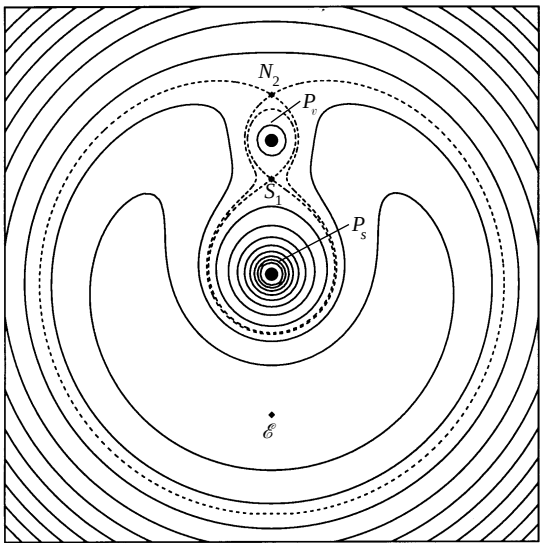


FIGURE 7. Characteristic streamline pattern associated with two point vortices (marked $P_v$ and $P_s$, respectively) in a co-rotating reference frame for the case $\gamma_v/\gamma_s = 0.2$ (see text for more details). The separatrices are indicated by the dashed lines. The hyperbolic points are marked by $S_1$ and $N_2$, respectively, whereas the elliptic point is marked by $\mathscr{E}$.

When a co-rotating coordinate system is taken, in which the motion is steady, the Eulerian velocity field is given by

$$u(x, y) = -\frac{\gamma_s y}{x^2 + y^2} - \frac{\gamma_v (y - y_0)}{(x - x_0)^2 + (y - y_0)^2} + \frac{\gamma_s y}{x_0^2 + y_0^2}, \tag{5.1}$$

$$v(x, y) = \frac{\gamma_s x}{x^2 + y^2} + \frac{\gamma_v (x - x_0)}{(x - x_0)^2 + (y - y_0)^2} - \frac{\gamma_s x}{x_0^2 + y_0^2}, \tag{5.2}$$

with $u$ and $v$ the velocity components in the $x$- and $y$-direction, respectively. The factors $2\pi$ have been included in the definitions of $\gamma_v$ and $\gamma_s$. The first term in each of the above equations corresponds to the shear flow, whereas the second term contains the contribution of the monopolar vortex. The third term arises due to the rotation of the reference system. From (5.1) and (5.2) the stream function can be derived, which may be written as

$$\psi(x, y) = -\frac{\gamma_s}{2} \ln \left[ \frac{x^2 + y^2}{x_0^2 + y_0^2} \right] - \frac{\gamma_v}{2} \ln \left[ \frac{(x - x_0)^2 + (y - y_0)^2}{x_0^2 + y_0^2} \right] + \frac{\gamma_s}{2} \frac{x^2 + y^2}{x_0^2 + y_0^2}. \tag{5.3}$$

Figure 7 shows a contour plot of the co-rotating stream function for the case $\gamma_v/\gamma_s = 0.2$. Two hyperbolic points (or stagnation points) can be identified, namely at $S_1$ and $N_2$, and one elliptic point, $\mathscr{E}$. Each hyperbolic point is associated with the self-intersection of a streamline: the inner separatrix $\Psi_1$, which has an eight-like shape and encloses each point vortex separately, and the outer separatrix $\Psi_2$, which surrounds both point vortices.

In order to determine the stream function values $\psi = \Psi_1$ and $\psi = \Psi_2$ at the separatrices, the positions of the hyperbolic points $S_1$ and $N_2$ have to be determined. When it is assumed that $x_0 = 0$, the hyperbolic points will lie on the $y$-axis due to the symmetry of the flow (see figure 7). The position of $S_1$ and $N_2$ can then be determined

by putting both (5.1) and (5.2) equal to zero, which yields

$$u = -\frac{\gamma_s}{y} - \frac{\gamma_v}{(y - y_0)} + \frac{\gamma_s y}{y_0^2} = 0, \tag{5.4}$$

$$v \equiv 0. \tag{5.5}$$

When the singular points $(0,0)$ and $(0, y_0)$ are excluded and the vortices do not coincide, (5.4) can be written as a cubic equation

$$\left(\frac{y}{y_0}\right)^3 - \left(\frac{y}{y_0}\right)^2 - \left(1 + \frac{\gamma_v}{\gamma_s}\right)\left(\frac{y}{y_0}\right) + 1 = 0, \tag{5.6}$$

which has three real and unequal roots (assuming that $\gamma_v/\gamma_s > 0$):

$$\frac{y_1}{y_0} = 2\left(\frac{4}{9} + \frac{1}{3}\frac{\gamma_v}{\gamma_s}\right)^{1/2} \cos\left(\frac{\alpha}{3} - \frac{2}{3}\pi\right) + \frac{1}{3}, \tag{5.7}$$

$$\frac{y_2}{y_0} = 2\left(\frac{4}{9} + \frac{1}{3}\frac{\gamma_v}{\gamma_s}\right)^{1/2} \cos\left(\frac{\alpha}{3}\right) + \frac{1}{3}, \tag{5.8}$$

$$\frac{y_3}{y_0} = 2\left(\frac{4}{9} + \frac{1}{3}\frac{\gamma_v}{\gamma_s}\right)^{1/2} \cos\left(\frac{\alpha}{3} + \frac{2}{3}\pi\right) + \frac{1}{3}, \tag{5.9}$$

in which

$$\cos\alpha = \frac{9(\gamma_v/\gamma_s) - 16}{6\sqrt{3}\left[\frac{4}{3} + \gamma_v/\gamma_s\right]^{3/2}}. \tag{5.10}$$

The positions $(0, y_1)$ and $(0, y_2)$ correspond to the hyperbolic points $S_1$ and $N_2$, respectively, whereas the position $(0, y_3)$ is related to the elliptic point $\mathscr{E}$. The stream function values $\Psi_i$ $(i = 1, 2)$ can now be determined by substituting $y_i$ $(i = 1, 2)$ into (5.3) and by setting $x_0 = 0$:

$$\Psi_i \equiv \psi(0, y_i) = -\gamma_s \ln\left|\frac{y_i}{y_0}\right| - \gamma_v \ln\left|\frac{y_i}{y_0} - 1\right| + \frac{\gamma_s}{2}\left(\frac{y_i}{y_0}\right)^2, \; i = 1, 2. \tag{5.11}$$

In order to get an idea of the shape of both separatrices, the stream function (5.3) will be rewritten as

$$\psi = -\gamma_s \ln\left(\frac{r}{r_0}\right) - \gamma_v \ln\left(\frac{R}{r_0}\right) + \frac{\gamma_s}{2}\left(\frac{r}{r_0}\right)^2, \tag{5.12}$$

where $r$ and $R$ are the radii with respect to the vortices $P_s$ and $P_v$, respectively, and $r_0$ is the distance between $P_s$ and $P_v$.

Now, on each separatrix, the extrema of $R$ can be found by substituting $\psi = \Psi_i$ into (5.12) and by taking the derivative of (5.12) with respect to $\theta$ (defined as in figure 8 *a*), which yields

$$\frac{\gamma_v}{R_i}\frac{\mathrm{d}R_i}{\mathrm{d}\theta} = \frac{\gamma_s}{2}\left[\frac{r_i^2 - r_0^2}{r_i^2 r_0^2}\right]\frac{\mathrm{d}(r_i^2)}{\mathrm{d}\theta}, \tag{5.13}$$

where $R_i$ $(i = 1, 2)$ is the radial distance between $P_v$ and an arbitrary point $(x_i, y_i)$ on the separatrix $\Psi_i$. Likewise, $r_i$ represents the radial distance between $P_s$ and $(x_i, y_i)$. By using the trigonometric relation $r_i^2 = R_i^2 + r_0^2 + 2R_i r_0 \sin\theta$ and setting $\mathrm{d}R_i/\mathrm{d}\theta = 0$, it can be derived that

$$\left[\left(r_0/r_i\right)^2 - 1\right]\cos\theta = 0. \tag{5.14}$$

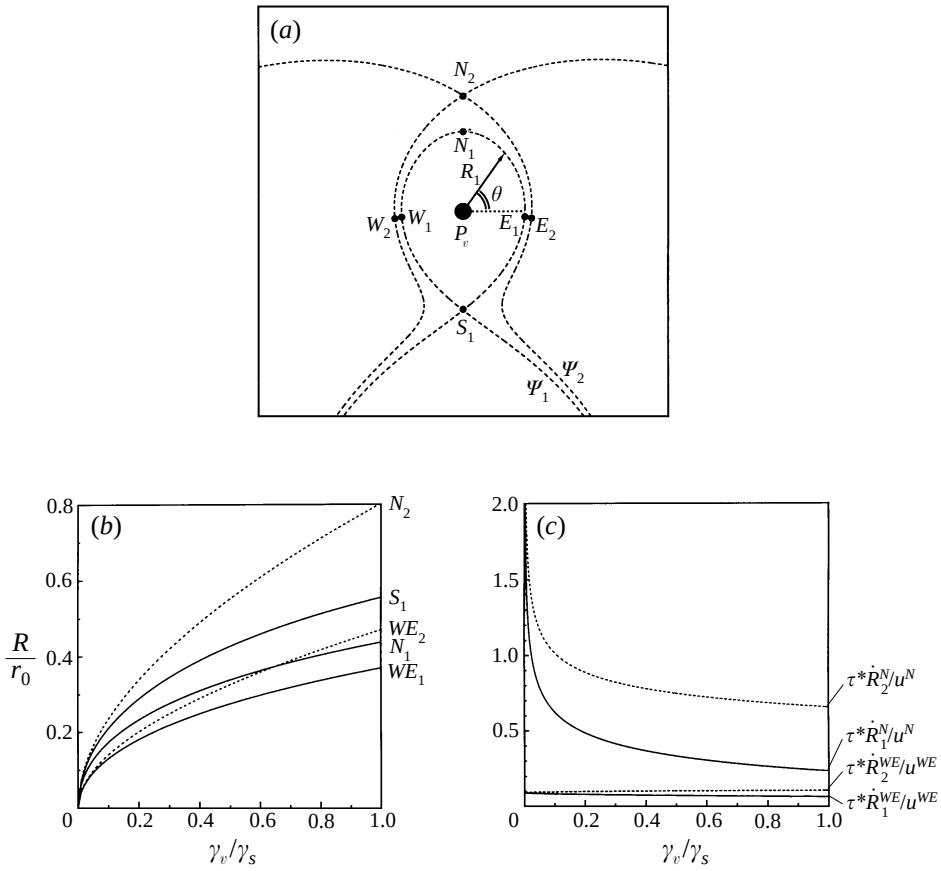


FIGURE 8. (*a*) Location of the extrema on the separatrices, along with the definitions of $R_1$ and $\theta$. (*b*) The relative radial distance $R/r_0$ of the extrema versus $\gamma_v/\gamma_s$. (*c*) Characteristic parameters at the extremal points as a function of $\gamma_v/\gamma_s$ (see text).

In other words, the extrema of $R_i$ should satisfy

$$r_i = r_0 \tag{5.15}$$

or

$$\theta = \tfrac{1}{2}\pi + n\pi, \tag{5.16}$$

respectively, where $n$ is an integer. Combination with (5.12) leads to the following relevant solutions for the extrema of $R$ on the separatrices:

$$\frac{R_i^W}{r_0} = \frac{R_i^E}{r_0} = \exp\left\{-\frac{\gamma_s}{\gamma_v}\left(\Psi_i - \frac{1}{2}\right)\right\}, \tag{5.17}$$

$$\frac{R_i^N}{r_0} = \exp\left\{-\frac{\gamma_s}{\gamma_v}\left[\Psi_i + \ln\left(1 + \frac{R_i^N}{r_0}\right) - \frac{1}{2}\left(1 + \frac{R_i^N}{r_0}\right)^2\right]\right\}, \tag{5.18}$$

where the superscripts refer to the positions of the extrema relative to the vortex $P_v$, as indicated in figure 8 (*a*). That is, $R_i^N$ is the distance in the 'Northward' direction from the vortex $P_v$ to the separatrix $\Psi_i$, and similarly for $R_i^E$, $R_i^S$ and $R_i^W$. Relation (5.18) is a transcendental equation which can be solved iteratively by common numerical techniques. Note that $R_2^N$ refers to the same position as $y_2$ in (5.8).

In figure 8 (*b*), the radial positions of the extrema are plotted as a function of $\gamma_v/\gamma_s$. The solid lines correspond to the inner separatrix ($\Psi_1$), whereas the dashed lines are related to the outer separatrix ($\Psi_2$). It is obvious that on the interval $0 < \gamma_v/\gamma_s < 0.65$

$$R_1^{WE} < R_2^{WE} < R_1^N < R_1^S < R_2^N, \tag{5.19}$$

whereas in the range $\gamma_v/\gamma_s > 0.65$

$$R_1^{WE} < R_1^N < R_2^{WE} < R_1^S < R_2^N. \tag{5.20}$$

Laboratory observations presented in § 4 have revealed that the monopolar vortex is characterized by a continuous spatial vorticity distribution and net circulation. Furthermore, it was observed that the vortex was deformed due to the presence of the background shear flow. Since the vorticity of a point vortex is concentrated in a singular point, the point vortex can essentially not be deformed. Therefore, a passive contour is defined around the point vortex in order to model the shape of the laboratory vortex. Initially, a circular contour may be chosen with radius $R_v$, which is large enough to ensure that for the corresponding distributed vortex $\omega(R_v)/\omega_m \ll 1$. The area enclosed by this passive contour will now be part of the model vortex.

Suppose that $R_v$ is defined such that $\omega(R_v)/\omega_m = \beta$, where $\beta$ is a constant that is much smaller than 1. Then, depending on the values of $R_v$ and $\gamma_v/\gamma_s$, three different initial situations may be considered, as shown in the upper row of figure 9, with the dashed lines denoting the separatrices. In situation A, the passive contour lies entirely inside separatrix $\Psi_1$, whereas in situation B, part of the model vortex is located between separatrices $\Psi_1$ and $\Psi_2$. In situation C, the vortex partly overlaps both separatrices. These three different situations that arise for different values of $R_v$ and $\gamma_v/\gamma_s$ can also be identified in figure 8 (*b*). Case A corresponds to the area below the curve $R_1^{WE}(\gamma_v/\gamma_s)$, whereas situation B corresponds to the area enclosed by the curves $R_1^{WE}(\gamma_v/\gamma_s)$ and $R_2^{WE}(\gamma_v/\gamma_s)$. Finally, the remaining area corresponds to situation C.

In order to investigate the behaviour of the vortex for the three different cases described above, the contour kinematics technique was applied here, which allows passive tracers (or nodes) that are positioned on a material contour to be followed. This technique is closely related to the contour dynamics method (see § 6), but the velocities used to advect the contour are prescribed rather than calculated from the contour position (as in contour dynamics). The displacement of each tracer was calculated by solving (5.1) and (5.2) with a Runge–Kutta method with variable time step and order (see Hairer, Nørsett & Wanner 1987). In order to maintain an accurate representation of the material contour, extra tracers were added during the time integration. Likewise, tracers were removed whenever possible to speed up the calculations. For a detailed description of this method, see Meleshko & van Heijst (1994). In the numerical simulations, the dimensionless time $t^* = t/T$ will be used, with $T = 2\pi r_0^2/\gamma_s$ the orbit period of point vortex $P_v$ around the centre of the flow field.

The typical calculated time evolution of the vortex is shown in column (*a*) of figure 9, with situation A taken as an initial condition. Since in a steady flow the separatrix acts as a barrier for passive fluid particles, the vortex is trapped within the area enclosed by $\Psi_1$. Owing to the elliptic-like shape of the streamlines, the blob of passive fluid is slightly deformed and two filaments arise which are being wrapped around the vortex. These filaments, however, never escape from the region bounded by the inner separatrix.

The advection of fluid with situation B as an initial condition is illustrated by the

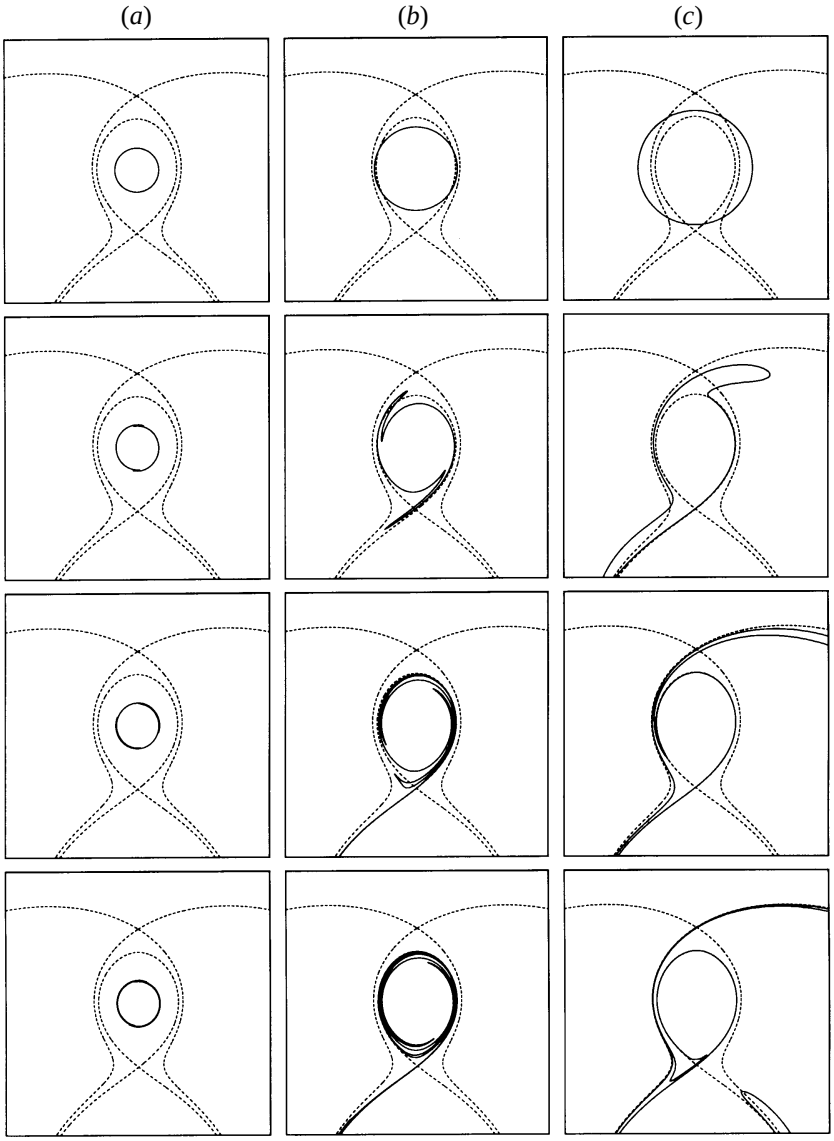


FIGURE 9. Calculated time evolution of passive tracers that are initially located on a circular contour for three different cases: $R_v/r_0 = 0.10$ (column *a*), $R_v/r_0 = 0.19$ (column *b*) and $R_v/r_0 = 0.26$ (column *c*). For each time series, $\gamma_v/\gamma_s = 0.2$ and the time interval between successive plots is 1/4 dimensionless time units.

sequence of plots shown in column (*b*) of figure 9. While most of the vortex area is still trapped inside the region enclosed by separatrix $\Psi_1$, both parts of the vortex which are located outside $\Psi_1$ are advected towards stagnation point $S_1$, giving rise to two tails which are expelled into the ambient flow as one filament.

When the vortex partly covers both separatrices (situation C), tracers that are located between both separatrices will be transported towards stagnation point $S_1$ (see column *c* in figure 9). This is also true for the tracers lying in the exterior region on the left-hand side of $\Psi_2$. However, the edge of the vortex on the right-hand side

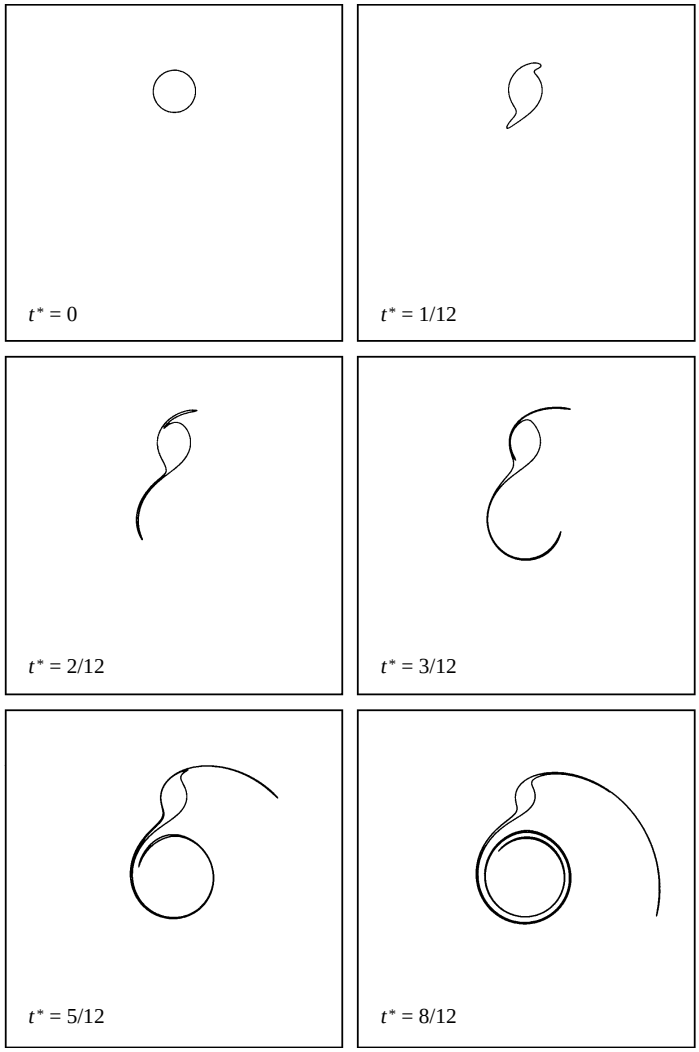


FIGURE 10. Temporal evolution of passive tracers for an exponentially decaying point vortex in an annular shear flow. Numerical parameters: $R_v/r_0 = 0.26$, $\gamma_0 = 0.32$ and $\tau^* = 0.43$.

of separatrix $\Psi_2$ will be advected towards stagnation point $N_2$, and hence form an additional tail, which is expelled as a second filament.

Thus far, attention has been restricted to steady flows. However, according to linear Ekman dynamics, monopolar vortices in rotating fluids decay exponentially in time, which was confirmed experimentally by Kloosterziel & van Heijst (1992). In order to examine the effect of the exponential decay of vorticity, $\gamma$ ($\equiv \gamma_v/\gamma_s$) is made time dependent according to

$$\gamma(t) = \gamma_0 \exp(-t/\tau), \tag{5.21}$$

where $\gamma_0$ represents the initial ratio between $\gamma_v$ and $\gamma_s$ (the latter being a constant due to the continuous forcing), and $\tau$ is the characteristic decay time.

Figure 10 shows a typical calculated evolution of the model vortex in the time-dependent velocity field, with situation C taken as an initial condition. In the initial stage of the evolution, the material contour is deformed in a similar manner as in the

stationary case (see column $c$ of figure 9). However, owing to the decay of $\gamma$ the area enclosed by separatrix $\Psi_1$ will shrink, which leads to the continuous feeding of the filament near stagnation point $S_1$. Also both separatrices will come closer together, which can be derived from figure 8 ($b$), so that the distance between the vortex core and the filament on its left-hand side becomes smaller. Moreover, when time increases, an anomalous tail appears close to stagnation point $N_2$ (at $t^* \approx 5/12$), which is entirely absent in the stationary case. Apparently, the expulsion of the anomalous tail is a property of the decaying vortex. From the last frame in figure 10 ($t^* = 8/12$) it can be seen that the anomalous tail is expelled into the ambient flow close to the second filament. The final stage of the evolution is characterized by the continuous depletion of the vortex core, while the area of the vortex core progressively decreases. Note that during the entire stripping process, the vortex core retains its perpendicular orientation to the shear flow direction.

In order to explain the appearance of the anomalous tail, it is convenient to define some average velocities in the narrow 'canal' between both separatrices:

$$u^E = \frac{\Psi_2 - \Psi_1}{R_2^E - R_1^E}, \tag{5.22}$$

$$u^N = \frac{\Psi_2 - \Psi_1}{R_2^N - R_1^N}, \tag{5.23}$$

$$u^W = \frac{\Psi_2 - \Psi_1}{R_2^W - R_1^W}. \tag{5.24}$$

These velocities can easily be calculated numerically by using (5.11), (5.17) and (5.18). Owing to the symmetry of the flow field, $u^E = u^W$ ($\equiv u^{WE}$).

Furthermore, the time derivatives of the extremal radii $R_i^{WE}$ and $R_i^N$ can be written as

$$\dot{R}_i^{WE} = \frac{\mathrm{d}R_i^{WE}}{\mathrm{d}\gamma}\dot{\gamma}, \tag{5.25}$$

$$\dot{R}_i^N = \frac{\mathrm{d}R_i^N}{\mathrm{d}\gamma}\dot{\gamma}, \tag{5.26}$$

respectively, where the dot represents differentiation with respect to time, and $\dot{\gamma} = -\gamma/\tau$ according to (5.21).

It may now be anticipated that all the fluid that crosses separatrix $\Psi_1$ will be carried away through stagnation point $S_1$ as long as $\dot{R}_1^{WE} \ll u^{WE}$ and $\dot{R}_1^N \ll u^N$, i.e. passive fluid is being advected quasi-steadily around separatrix $\Psi_1$. However, when one of these conditions is not satisfied, fluid may leak through separatrix $\Psi_2$. In order to investigate whether these conditions are fulfilled during the decay process, the ratios $\tau^* \dot{R}_i^{WE}/u^{WE}$ and $\tau^* \dot{R}_i^N/u^N$ (with $\tau^* = \tau/T$) have been plotted versus $\gamma$ in figure 8 ($c$) for $i = 1, 2$.

Owing to the decay of $\gamma$, fluid will continuously leak through separatrix $\Psi_1$. Supposing that $\tau^* \approx O(1)$ (which is the case for the numerical results shown in figure 10), it is clear from figure 8 ($c$) that fluid crossing the inner separatrix near one of the extremal points $W_1$ or $E_1$ is advected adiabatically towards the stagnation point $S_1$ for all values of $\gamma$. Also near extremum $N_1$ the fluid is removed in a quasi-steady way, except for small values of $\gamma$. The latter restriction explains the occurrence of the anomalous tail in the contour kinematics simulation: owing to the smallness of velocity $u^N$ compared to both $\dot{R}_1^N$ and $\dot{R}_2^N$, stagnation point $N_2$ penetrates into the core of the model vortex, which consequently leads to the expulsion of the anomalous

tail. Although $\dot{R}_2^N/u^N \approx O(1)$ for the entire range of $\gamma$, stagnation point $N_2$ can never reach the boundary of the vortex as long as the fluid near separatrix $\Psi_1$ is advected quasi-adiabatically, i.e. $\dot{R}_1^N/u^N \ll 1$.

Additional numerical simulations were carried out with situation A or B as an initial condition; apart from the absence of the first filament near stagnation point $N_2$, similar results were obtained to those shown in figure 10.

The experimental observations shown in figure 5 are in very good qualitative agreement with the numerical results presented in figure 10 throughout the major part of the vortex evolution. This is evident from the filaments that appear on both sides of the vortex, and the shape and orientation of the vortex core. This similarity is quite striking, keeping in mind that real vortices are characterized by a continuous spatial vorticity distribution, whereas this is not the case for a point vortex. Even so, the final breaking of the laboratory vortex cannot be explained by the simple point-vortex model. Therefore, in the next section, the effect of the continuous vorticity distribution will be examined.

## 6. The influence of distributed vorticity

The effect of the vorticity distribution on the evolution of the monopolar vortex in the irrotational annular shear flow was investigated by applying the contour dynamics approach. The contour dynamics method is based on the Euler equations in two dimensions and requires a discretization of the spatial vorticity distribution, i.e. the spatial vorticity profile is represented by concentric contours between which the vorticity is uniform (see Zabusky, Hughes & Roberts 1979). The contours are modelled by nodes and can be followed in time by performing a time integration of the total velocity field which consists of two contributions: the velocity field associated with the discretized vortex, which can be found by solving Poisson's equation, and the background velocity field, which may be calculated analytically. Like in the contour kinematics approach, nodes are added and removed in the course of the calculation, depending on the local deformation of the contours.

As an initial condition, the vorticity profile (4.4) was taken, which was represented by seven equidistant vorticity contours. The uniform vorticity $\omega_i$ at each vorticity level $i$ was chosen such that $\omega_i = \Gamma_i/A_i$, where $A_i$ represents the area enclosed by the bounding contours $i$ and $i-1$, and $\Gamma_i$ is the corresponding circulation associated with the distributed vortex (it should be noted that $i = 0$ corresponds to the centre of the vortex). The radius of the third contour was taken equal to $L_v$ (the characteristic length scale of the vortex), whereas the radius of the exterior contour $R_v$ was chosen equal to $2.6L_v$. The flow surrounding the exterior contour was assumed irrotational. As a result, the total circulation of the discretized vortex is $0.9988\gamma$, which is almost equal to the strength $\gamma$ of the distributed vortex. The linear Ekman decay was mimicked by allowing each level of uniform vorticity to decay according to $\omega_i(t) = \omega_i(0)\exp(-t/\tau)$, where $\omega_i(0)$ represents the initial vorticity value.

The typical evolution of the vorticity contours is shown in figure 11, where the same initial values for $\gamma$ and $\tau$ have been used as in the contour kinematics calculations. These parameters are based on quantitative measurements of the sink-vortex characteristics in a still ambient fluid just after the forcing device was removed from the tank. Since the scaled radius of the exterior vorticity contour $R_v/r_0$ is equal to that of the material contour shown in figure 10, both contours may be compared with each other, and one can observe a remarkable resemblance during most of the evolution. Apparently, the filaments being detached from the discretized vortex contain

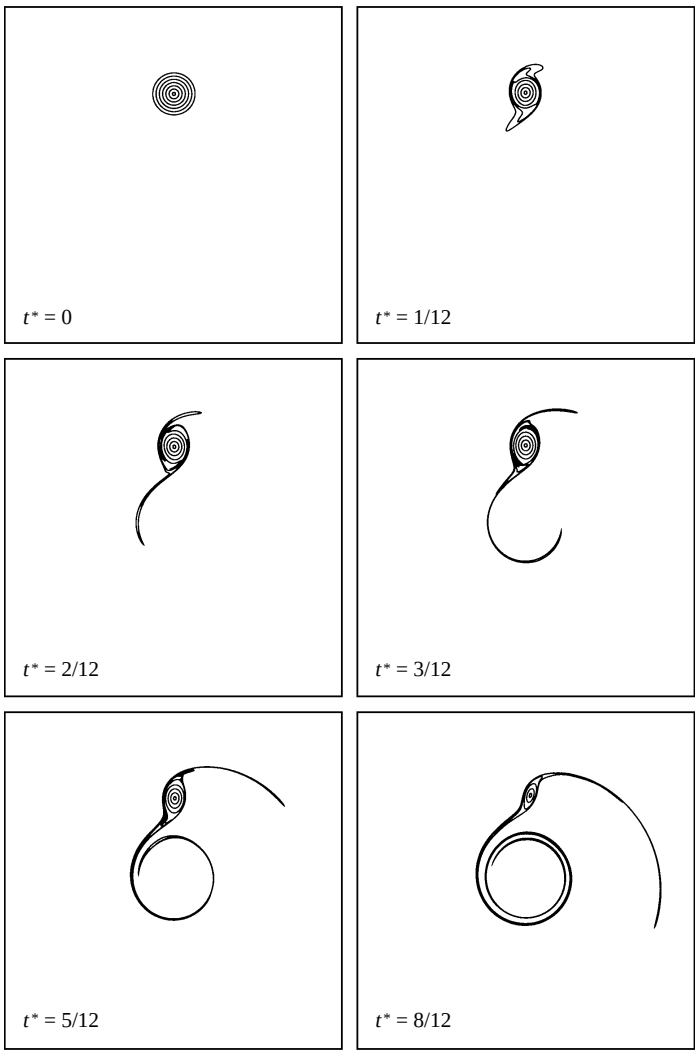


FIGURE 11. Time series of the evolving vorticity contours in an annular shear flow as obtained by the contour dynamics method (see text for more details). Numerical parameters: $R_v/r_0 = 0.26$ ($L_v/r_0 = 0.10$), $\gamma_0 = 0.32$ and $\tau^* = 0.43$.

a negligible amount of vorticity, because otherwise, the circulation of the remaining vortex would decrease faster than exponentially. In the final stage of the evolution, however, the contour dynamics results show that the vortex is torn apart by the shear flow, while the stripping process around the point vortex continues indefinitely. This discrepancy may be understood by noting that in general, vortices with a finite vorticity distribution are overcome by the shear flow at some critical value $(e/\omega_m)_c$; that is, when the local strain rate $e$ (which is equal to $\gamma_s/r_0^2$ for the annular shear flow described in this paper) is sufficiently large compared to the maximum vorticity $\omega_m$ of the vortex. When the ratio $e/\omega_m$ exceeds this critical breaking value the stagnation points will vanish, resulting in the final elongation of the entire vortex. On the other hand, the point vortex cannot be broken by definition, since it contains infinite vorticity in a singular point. Consequently, the stripping process persists forever.

The contour dynamics results are also in very good qualitative agreement with the laboratory observations depicted in figure 5 during the entire evolution of the vortex. It is observed that both experimentally and numerically, the vortex remains oriented perpendicular to the shear flow direction for a considerable time. In an analytical study by Kida (1981), it was shown that this orientation corresponds to the steady state of an elliptic patch of uniform vorticity embedded in a linear shear flow. Moreover, contour dynamics simulations by Legras & Dritschel (1993, 1994) have revealed that in a slowly growing linear shear flow, distributed vortices evolve along quasi-stationary states for a considerable time until the vortex is torn apart by the ambient flow. Although the annular shear as described in the present study is characterized by a nonlinear radial velocity distribution, the vortex core is apparently insensitive to the exact shape of the background velocity profile. The reason for this may be that locally, the velocity profile of an arbitrary shear flow is always close to linear.

The quasi-adiabatic stripping process described above is very similar to that observed in the laboratory by Trieling, Beckers & van Heijst (1997) for a monopolar vortex subjected to a pure strain flow, in which case the vortex is oriented at an angle of 45° with respect to the horizontal strain axis. The similarity is not surprising since in both cases the vortex is oriented at 45° with respect to the principal axes of the strain. This may also explain the final orientation of the vortex as shown in figures 5 and 11, which corresponds to the elongation of the vortex along one of these principal axes.

Although the evolution of the numerically obtained vorticity contours is very similar to the evolving dye pattern as observed in the laboratory, the Ekman time $T_E$ is about twice as large as the e-folding decay time $\tau$ corresponding to the numerical results depicted in figures 10 and 11. Therefore, similar numerical simulations were performed with $\tau = T_E$. Again, the results obtained by the contour kinematics technique were in excellent agreement with the contour dynamics calculations for a considerable time. However, the laboratory observations revealed a much faster evolution compared with these latter numerical results.

Since the initial Rossby number was $O(1)$ in the rotating fluid experiments, it is very likely that the accelerated evolution of the laboratory vortex is due to nonlinear effects, as discussed in § 4. Accordingly, the evolution of the vortex is initially much faster than expected from an exponential vorticity decay. Furthermore, the Ekman layer at the bottom wall drives a secondary motion that will result in an additional radial growth of the vortex. Although this effect may be neglected in the linear case, it is important when nonlinear effects come about. Both the faster decay of vorticity and the growing vortex size may enhance the advection of vorticity across the inner separatrix, which leads to an accelerated erosive decay of the vortex.

Another reason for the accelerated evolution of the laboratory vortex might be that the vorticity decay is enhanced by viscous effects. Indeed, it was shown in a numerical study by Mariotti, Legras & Dritschel (1994) that the combination of vortex stripping and diffusion may speed up the stripping process and consequently the decay of the vortex. However, considering the initial ratio of the Ekman decay time and the characteristic diffusive time $T_E/T_d \approx 0.2$, where $T_d \equiv r_m^2/\nu$, diffusion will only be of secondary importance.

Furthermore, it should be stressed that the initial vortex parameters used in the numerical calculations have been obtained from measurements in a still ambient fluid. It may well be that the generation of the sink vortex is affected by the shear flow. However, close inspection of the spiralling dye structure revealed that in the initial

stage $Ro$ is still $O(1)$. Quantitative measurements of the flow field have confirmed this assertion. Finally, the effect of the sidewall may probably be neglected, since the core of the vortex is being advected with the local velocity associated with the shear flow.

## 7. Conclusions

Rotating fluid experiments described in this paper have revealed the stripping of a monopolar vortex in an irrotational annular shear flow. In contrast to uniform shear flows, the vorticity filaments were observed to be asymmetrically attached to the vortex core. Theoretically, the asymmetric stripping process can be explained in terms of the streamlines in a co-rotating frame, as obtained by modelling both the monopolar vortex and the irrotational shear flow simply by point vortices. The co-rotating streamline pattern is characterized by two nested separatrices, each of which contains one stagnation point. Combination of the point-vortex model with the contour kinematics technique revealed a very good qualitative agreement with the laboratory observations for the quasi-stationary part of the vortex evolution. Contour dynamics simulations have shown that the final breaking of the vortex is caused by the continuous spatial distribution of vorticity. The temporal evolution of the laboratory vortex may be accelerated by nonlinearities and lateral diffusion, effects which were not incorporated in the contour dynamics model. However, it is expected that these mechanisms do not affect the basic evolution characteristics of the monopolar vortex in an irrotational annular shear flow.

We would like to thank Pauline Vosbeek for her kind willingness to provide us with the contour dynamics code, and to Professor Vyacheslav V. Meleshko and Dr Alexei Galaktionov for providing software to perform contour kinematics simulations. One of the authors (R.R.T.) gratefully acknowledges financial support by the Foundation for Fundamental Research on Matter (FOM) of the Netherlands Organization for Scientific Research (NWO).

## REFERENCES

Brickman, D. & Ruddick, B. R. 1990 The behavior and stability of a lens in a strain field. *J. Geophys. Res.* **95**, 9657–9670.

Dalziel, S. 1992 *DigImage. Image Processing for Fluid Dynamics.* Cambridge Environmental Research Consultants Ltd.

Dritschel, D. G. 1989 Strain-induced vortex stripping. In *Mathematical Aspects of Vortex Dynamics* (ed. R. E. Caflisch), pp. 107–119. Society of Industrial and Applied Mathematics.

Dritschel, D. G. & Waugh, D. W. 1992 Quantification of the inelastic interaction of unequal vortices in two-dimensional vortex dynamics. *Phys. Fluids* A **4**, 1737–1744.

Greenspan, H. P. 1968 *The Theory of Rotating Fluids.* Cambridge University Press.

Hairer, E., Nørsett, S. P. & Wanner, G. 1987 *Solving Ordinary Differential Equations — I: Nonstiff Problems.* Springer, Berlin.

Heijst, G. J. F. van 1984 Source–sink flow in a rotating cylinder. *J. Engng Maths* **18**, 247–257.

Hide, R. 1968 On source–sink flows in a rotating fluid. *J. Fluid Mech.* **32**, 737–764.

Hide, R. 1977 Experiments with rotating fluids. *Q. J. R. Met. Soc.* **103**, 1–28.

Kida, S. 1981 Motion of an elliptic vortex in a uniform shear flow. *J. Phys. Soc. Japan* **50**, 3517–3520.

Kloosterziel, R. C. & Heijst, G. J. F. van 1992 The evolution of stable barotropic vortices in a rotating free-surface fluid. *J. Fluid Mech.* **239**, 607–629.

Kuo, H.-H. & Veronis, G. 1971 The source–sink flow in a rotating system and its oceanic analogy. *J. Fluid Mech.* **45**, 441–464.

Lamb, H. 1932 *Hydrodynamics*, 6th edn. Cambridge University Press.

Legras, B. & Dritschel, D. G. 1993 Vortex stripping and the generation of high vorticity gradients in two-dimensional flows. *Appl. Sci. Res.* **51**, 445–455.

Legras, B. & Dritschel, D. G. 1994 Vortex stripping. In *Modelling of Oceanic Vortices* (ed. G. J. F. van Heijst), pp. 51–59. North Holland.

Legras, B., Santangelo, P. & Benzi, R. 1988 High-resolution numerical experiments for forced two-dimensional turbulence. *Europhys. Lett.* **3**, 811–818.

Mariotti, A., Legras, B. & Dritschel, D. G. 1994 Vortex stripping and the erosion of coherent structures in two-dimensional flows. *Phys. Fluids* **6**, 3954–3962.

McWilliams, J. C. 1984 The emergence of isolated coherent vortices in turbulent flows. *J. Fluid Mech.* **146**, 21–43.

Melander, M. V., Zabusky, N. J. & McWilliams, J. C. 1987 Asymmetric vortex merger in two dimensions: Which vortex is "victorious"? *Phys. Fluids* **30**, 2610–2612.

Melander, M. V., Zabusky, N. J. & McWilliams, J. C. 1988 Symmetric vortex merger in two dimensions: causes and conditions. *J. Fluid Mech.* **195**, 303–340.

Meleshko, V. V. & Heijst, G. J. F. van 1994 Interacting two-dimensional vortex structures: point vortices, contour kinematics and stirring properties. *Chaos, Solitons & Fractals* **4**, 977–1010.

Nguyen Duc, T. & Sommeria, J. 1988 Experimental characterization of steady two-dimensional vortex couples. *J. Fluid Mech.* **192**, 175–192.

Overman, E. A. & Zabusky, N. J. 1982 Evolution and merger of isolated vortex structures. *Phys. Fluids* **25**, 1297–1305.

Paihua Montes, L. 1978 Methodes numériques pour le calcul de fonctions-spline à une ou plusieurs variables. Thèse de $3^e$ cycle, Université de Grenoble, France.

Stewartson, K. 1957 On almost rigid rotations. *J. Fluid Mech.* **3**, 17–26.

Trieling, R. R., Beckers, M. & Heijst, G. J. F. van 1997 Dynamics of monopolar vortices in a strain flow. *J. Fluid Mech.* **345**, 165–201.

Zabusky, N. J., Hughes, M. H. & Roberts, K. V. 1979 Contour dynamics for the Euler equations in two dimensions. *J. Comput. Phys.* **30**, 96–106.